Cytometry
PART A
Journal of the
International Society for
Advancement of Cytometry

Imaging of Dense Cell Cultures by Multiwavelength Lens-Free Video Microscopy

C. Allier,[1,2]* S. Morel,[1,2] R. Vincent,[1,2] L. Ghenim,[1,3,4,5] F. Navarro,[1,2] M. Menneteau,[1,2] T. Bordy,[1,2] L. Hervé,[1,2] O. Cioni,[1,2] X. Gidrol,[1,3,4] Y. Usson,[1,6] J.-M. Dinten[1,2]

[1]Universite Grenoble Alpes, Grenoble, F-38000, France

[2]CEA LETI MINATEC Campus, Grenoble, F-38054, France

[3]CEA BIG Biologie à Grande Echelle, Grenoble, F-38054, France

[4]INSERM, U1038, Grenoble, F-38054, France

[5]CNRS, FR CNRS 3425, Grenoble, F-38000, France

[6]TIMC-IMAG, Grenoble, F-38000, France

*Correspondence to: C. Allier; Universite Grenoble Alpes, Grenoble, F-38000, France. E-mail: cedric.allier@cea.fr

The authors declare that they have no conflicts of interest.

ISAC
International Society for Advancement of Cytometry

● **Abstract**

They present results for lens-free microscopy for the imaging of dense cell culture. With this aim, they use a multiwavelength LED illumination with well separated wavelengths, together with the implementation of an appropriate holographic reconstruction algorithm. This allows for a fast and efficient reconstruction of the phase image of densely packed cells (up to 700 cells/mm^2) over a large field of view of 29.4 mm^2. Combined with the compactness of the system which fits altogether inside an incubator, lens-free microscopy becomes a unique tool to monitor cell cultures over several days. The high contrast phase shift images provide robust cell segmentation and tracking, and enable high throughput monitoring of individual cell dimensions, dry mass, and motility. They tested the multiwavelength lens-free video-microscope over a broad range of cell lines, including mesenchymal, endothelial, and epithelial cells. © 2017 International Society for Advancement of Cytometry

INTRODUCTION

PROGRESS in biology has often been correlated with advances in microscopy. The majority of modern-day microscopic developments focus on increasing resolution. We can now visualize cells and tissues with unprecedented detail. Unfortunately, this is usually achieved at the expense of cost, invasiveness, compactness, simplicity, and/or field of view (FOV). As such, label-free microcopy techniques offering a large field of view are complementary to high resolution microscopy. Examples of such techniques are real-space (1) and Fourier (2) ptychography imaging, that have been developed to perform label free and high-contrast imaging of cell culture with low numerical aperture objectives (0.2–0.4 NA). A phase retrieval algorithm without support mask is used to recover the high contrast phase images at a resolution of approximately 1 μm with a large FOV [2.1 mm $\times$ 1.8 mm, (2)]. Recently such a system has been designed to fit inside an incubator, and offers an even larger FOV (5.7 mm $\times$ 4.3 mm) (3). An alternative to maximize the available field of view together with a small footprint is lens-free microscopy (4–6). It comprises a computational reconstruction of the object from its recorded hologram intensity. The hardware setup is light: a coherent point source illuminates the object located at distance l from the source, and the detector records the hologram intensity at a distance Z, with $l \gg Z$ (Fig. 1a). The hologram is then captured by a CMOS sensor located as close as possible to the sample, thus allowing wide field imaging over the whole sensor area. The sample image is recovered numerically with a phase retrieval algorithm (7–9), which usually requires a support mask of the object in order to impose shape and size constraints. Such algorithms are efficient to recover the amplitude and phase of isolated cells (10–13), but are limited to disperse cell cultures, with densities of
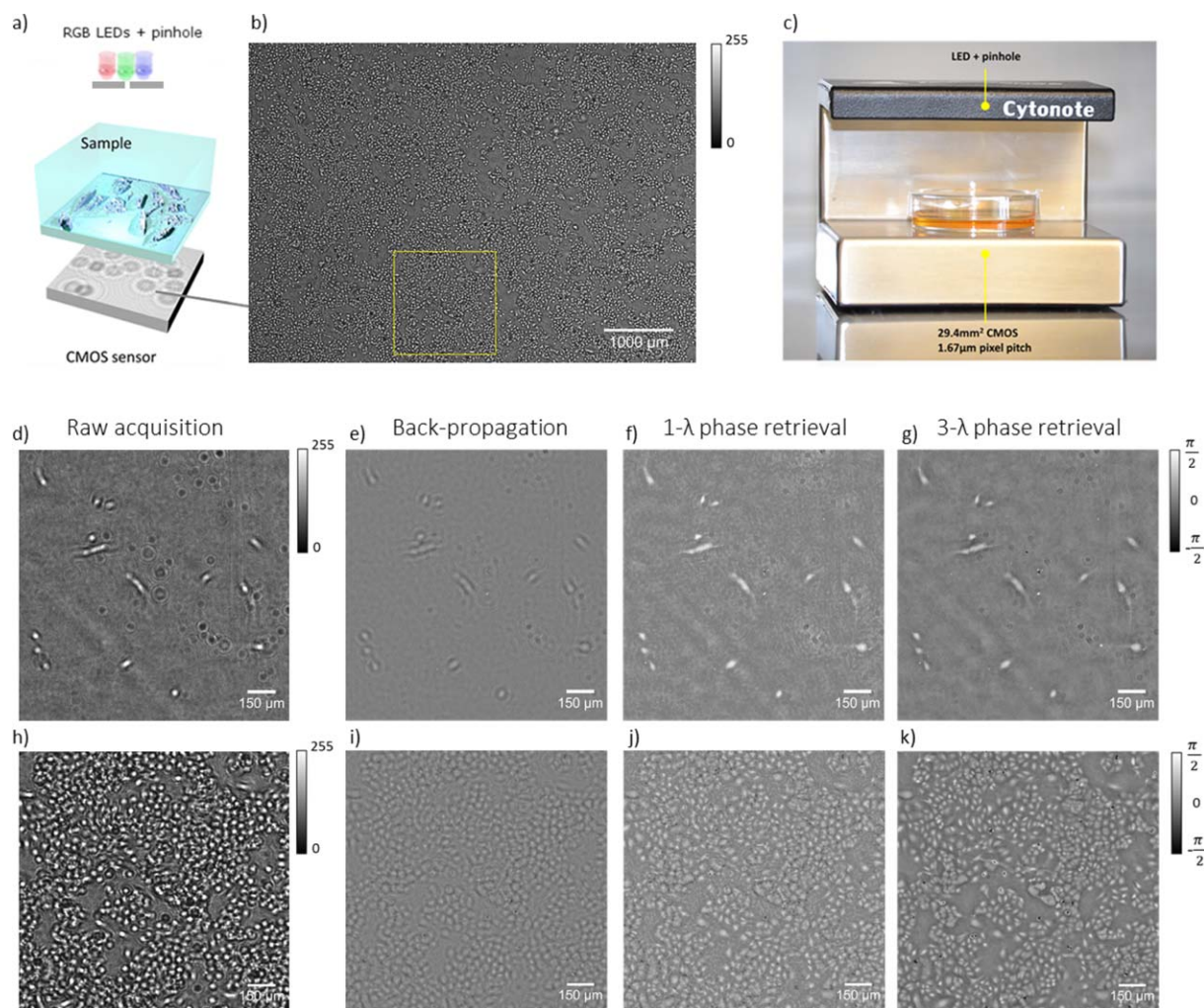
Figure 1. (a) Schematic of the lens-free microscopy acquisition setup. (b) Example of the full field of view raw acquisition of a culture of primary human umbilical vein endothelial cells. (c) Picture of the lens-free video microscope (Cytonote from Iprasense, Montpellier, France). It uses a CMOS image sensor with a pixel pitch of 1.67 μm and an imaging area of 6.4 mm $\times$ 4.6 mm = 29.4 mm^2. Illumination is provided by a multicolored RGB LEDs along with a pinhole placed at a distance of approximately 5 cm from the sample. The picture shows the lens-free video microscope imaging a cell culture in Petri dish (35 mm diameter). (d) and (h) Raw lens-free acquisitions (blue channel, detail of the full field of view) of a culture of A549 cells at low and high density ($\sim$675 cells/mm^2), respectively. (e) and (i) Reconstructed phase images obtained using the simple back propagation algorithm on (d) and (h), respectively. (f) and (j) Reconstructed phase images obtained using the one-wavelength phase retrieval algorithm applied to (d) and (h), respectively. (g) and (k) Reconstructed phase images obtained using the multiwavelength phase retrieval algorithm applied to (d) and (h), respectively. All reconstructed phase images are shown without phase unwrapping. [Color figure can be viewed at wileyonlinelibrary.com]

approximately 20 cells/mm^2 (10). In order to work on dense samples for which the definition of a mask is inaccurate, another class of reconstruction algorithms has been developed to use the information from multiple acquisitions. Pixel super-resolution (14) and multiheight acquisitions (15) have been used to image dense biological samples and reach sub-pixel resolution on, for example, unstained Pap smear and stained blood smears. These methods cannot, however, be applied to the live-monitoring of cell culture owing to the large number of required acquisitions. More recently, an approach based on the use of four pigtailed laser in the range of 640–660 nm has demonstrated the possibility to use four acquisitions only to image and monitor cell culture up to a density of approximately 80 cells/mm^2 (16).

In the present manuscript, we describe a lens-free microscopy setup based on the use of three multicolored LEDs delivering red, green, blue illuminations, together with the implementation of a reconstruction algorithm inspired from digital in-line holography (17). With this setup, we demonstrate the possibility to image and monitor cell culture across a field of view (FOV) of 29.4 mm^2, up to densities of approximately 700 cells/mm^2 for cell counting. Combined with the compactness of the system which fits altogether inside an incubator, we can monitor cells in cultures over several days, and follow the evolution in time of their morphology from low densities up to confluence. The high contrast phase shift images provide robust cell segmentation and tracking up to densities of approximately 350 cells/mm^2 and enable

Cell Cultures by Lens-Free Microscopy

high throughput monitoring of individual cell dimensions, dry mass and motility. We tested this multiwavelength video lens-free microscopy over a broad range of cell lines, including mesenchymal, endothelial, and epithelial cells.

MATERIALS AND METHODS

Cell Culture

HUVECs and 3T3 cell lines were, respectively, purchased from Millipore and ATCC. Experimental cultures were prepared from deep-frozen stock vials, and maintained in a sub-confluent state in culture Petri Dish (113 cm^2) coated with fibronectin for HUVECs and uncoated for 3T3 under a humidified (90%) atmosphere of 95% air/5% CO_2 at 37°C. Cells were grown in EndoGro basal medium supplemented with 5 ng/mL of rhVEGF, rhEGF, rhFGFb, respectively, 15 ng/mL rh IGF-1, 10 mM L-glutamine, 0.75U/mL heparin sulfate, 1 μg/mL hyroscortisone hemisucinate, 50 μg/mL ascorbic acid and 2% FBS or DMEM supplemented with 10% of newborn calf serum for HUVECs and 3T3, respectively. Culture medium is changed every second day. About 10^5 cells (HUVECs or 3T3) were seeded in 35 mn Petri Dish in 1 mL of their respective complete medium and monitored through lens-free video microscopy.

For fixation and DAPI staining, cells previously seeded on D-Poly-lysine coated coverglass slides were washed in warm (37°C) PBS, and soaked in PFA (2% paraformaldehyde in PBS) for 20 mn at 37°C. The fixed samples were then rinsed three times for 5 minutes with PBS. The cells were further permeabilized using a solution of 0.2% Triton in PBS for 3 minutes. Finally, the cells were washed three times for 5 minutes with PBS, and stained for nuclei with DAPI using Vectashield^{TM} mounting medium according to manufacturer instructions (Vector Laboratories, USA).

Lens-Free Video Microscopy

Image acquisition was performed with a Cytonote lens-free video microscope (Iprasense, France). It was inspired by the lens-free imaging system described by Su et al. (16), which was modified to perform continuous monitoring inside an incubator at a controlled temperature and humidity (Fig. 1). It uses a CMOS image sensor with a pixel pitch of 1.67 μm and an imaging area of 6.4 × 4.6 mm^2. Multiple wavelength illumination is provided by a multichip LEDs delivering red, green and blue illumination. The wavelengths are centered, respectively, on 636, 521, and 452 nm, with a spectral bandwidth of, respectively, 25, 45, and 25 nm. The RGB LEDs is located above a 150 μm pinhole at a distance of approximately 5 cm from the cells. The CMOS sensor is put in contact with the cell culture recipient. The distance between the cells and the CMOS sensor varies between 1 and 2 mm depending on the type of cell culture recipient, for example, Petri dish or multiwells plate.

Microscopy

Digital holographic microscopy was performed with a Lyncée Tec$^®$ Transmission microscope (DHM), using a ×5 objective (NA 0.12) and a laser of 647 nm. Fluorescence and bright-field microscopy was performed with a Zeiss Axioplan microscope using a ×20 objective (NA 0.4). Phase contrast microscopy was performed with an Olympus IXS1 microscope using a ×10 objective (NA 0.25) and an Olympus IX73 microscope using a ×10 objective (NA 0.3).

RESULTS AND DISCUSSION

Multiwavelength Holographic Reconstruction of Adherent Cells

The lens-free video microscope is placed inside the incubator and the culture dish containing the cells is set on top of the CMOS sensor (Fig. 1). The lens-free imaging optical setup does not acquire an image of the cell but the holographic interference pattern formed by the interference of the semi-coherent light scattered by the cells and the light passing directly from the source to the image sensor. A reconstruction algorithm is then used to recover the phase image of the cells from their interference holographic patterns. A simple holographic reconstruction method consists in back-propagating the light intensity recorded by the sensor using the Fresnel function (Fig. 1 and supplementary information). The result is a complex image of the cell which is however strongly affected by the so-called "twin image," an artifact that results from a lack of phase information in the acquisition process. This is a well-known problem that can be tackled with a phase retrieval algorithm (7). A simple phase-retrieval algorithm consists in propagating iteratively the image back and forth between the sensor and object planes with a support mask applied to the complex image in the object plane, in order to filter out the "twin-image" contribution (Supporting Information Fig. S2). In the case of adherent cells, it appears that the signal to noise ratio of the complex cell image obtained after a single back-propagation is too low to properly define such a mask (Figs. 1e–2i). Hence, for one-wavelength holographic reconstruction, we used the algorithm described in (18), which also propagates the image back and forth between the sensor and object planes, but this time with a positivity constraint applied on the reconstructed phase image while the reconstructed modulus image is set to 1 (Figs. 1f–1j; Supporting Information Fig. S2 and Supporting Information). These constraints reflect the fact that adherent cells can be considered as transparent objects. At low density (<20 cells/mm^2), this algorithm is efficient in diminishing the "twin-image" contribution and hence recovers the overall shape of the cells (Fig. 1f). At larger densities, however, the one-wavelength holographic reconstruction algorithm fails to properly recover the cell shape (Fig. 1j). The "twin-image" contribution is reduced but the reconstructed phase image is blurred and noisy, leading to inaccurate segmentation and tracking.

With the multiwavelength reconstruction algorithm (see Supporting Information Fig. S3), the reconstructed phase image of the cells is noticeably improved, in particular at large cell densities (Figs. 1g–1k, 2a and 2b). The multiwavelength reconstruction algorithm is based on recording holograms at different illumination wavelengths. The holograms are separately back-propagated to the object plane for the respective
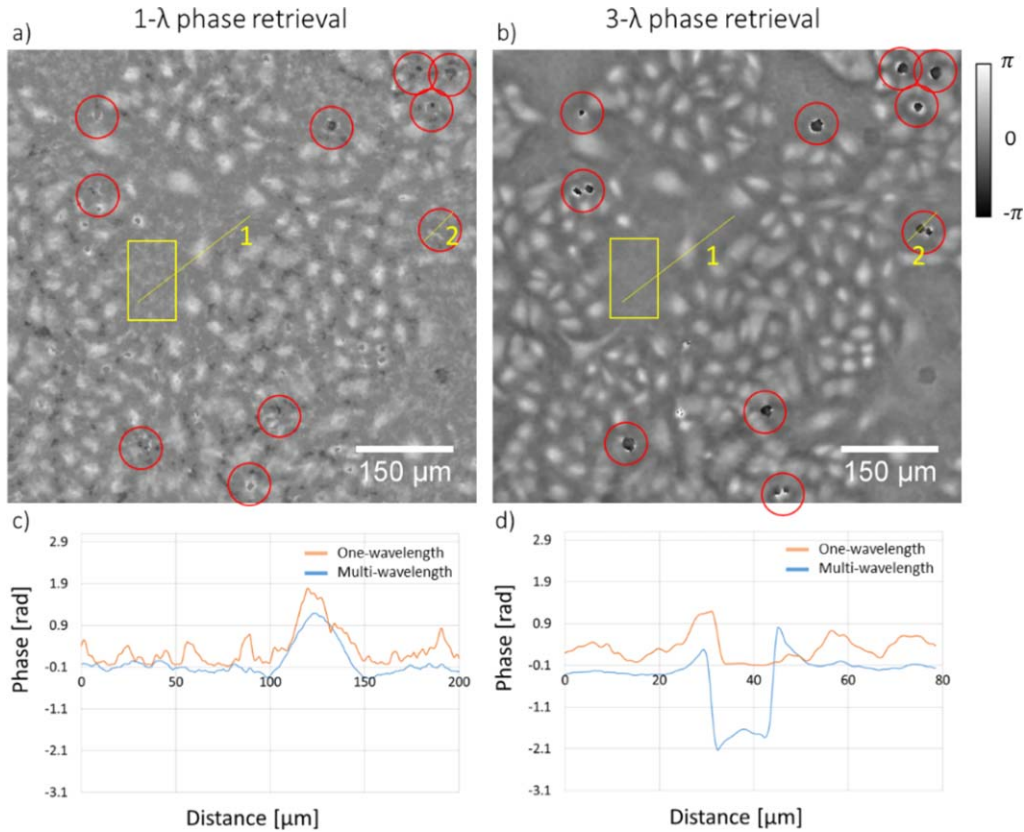
Figure 2. Comparison between the one-wavelength and the multiwavelength holographic reconstruction algorithms image at large cell density (~500 cells/mm^2, manual counting). (a) Reconstructed phase image of a culture of A549 cells (blue channel) obtained with the one-wavelength holographic reconstruction algorithm. (b) Reconstructed phase image of the region shown in (a) obtained with the multi-wavelength holographic reconstruction algorithm. The reconstructed phase images in (a) and (b) are shown without phase unwrapping. (c, d) Phase profile measured on a single cell [yellow line 1 in (a) and (b)] for the two different holographic reconstruction algorithms. The signal to noise ratio measured on the single cell is about 13.4 with the multiwavelength holographic reconstruction algorithm to be compared with 7.7 with the one-wavelength algorithm. Signal-to noise ratio being measured as the amplitude of the phase profile (c) divided by the noise measured in the background of the reconstructed image [yellow box in (a) and (b)]. In (b), dividing cells are clearly visible (red circles). They appear as black owing to a strong phase shift which results into phase wrapping. (d) Phase profile measured on a dividing single cell [yellow line 2 in (a) and (b)] for the two different holographic reconstruction algorithms. [Color figure can be viewed at wileyonlinelibrary.com]

illumination wavelengths. A new phase $\varphi^{\lambda_j}_{new}$ is calculated according to the reconstructed phase φ^{λ_i} obtained at the three wavelengths:

$$\varphi^{\lambda_j}_{new} = \frac{1}{3\lambda_j} \sum_{i=1}^{3} \varphi^{\lambda_i} . \lambda_i \qquad (1)$$

where λ_i are the three different wavelengths. Similarly a new modulus $m^{\lambda_j}_{new}$ is calculated according to the reconstructed modulus m^{λ_i} obtained at the three wavelengths:

$$m^{\lambda_j}_{new} = \frac{1}{3} \sum_{i=1}^{3} m^{\lambda_i} \qquad (2)$$

This calculation of a new complex cell image $m^{\lambda_j}_{new}.e^{i\varphi^{\lambda_j}_{new}}$ allows us to robustly average out the "twin-image" if the three wavelengths are well separated (Supporting Information Fig. S4). This is because the "twin-image" is more wavelength-dependent than the reconstructed complex cell image, the

latter sharing common features at the different illumination wavelengths. This calculation is iterated, by propagating the image back and forth between the sensor and object, and the reconstructed phase images in the red, green, and blue channel are finally obtained by back-propagating the refined complex amplitude to the object plane. As a result, with the multiwavelength reconstruction algorithm, the "twin-image" in the reconstructed phase image is drastically altered. Figure 2c shows that the signal-to-noise ratio measured on a single A549 cell is about 13.4 with the multiwavelength algorithm compared to 7.7 with the one-wavelength algorithm.

We note that the multiwavelength algorithm allows us to distinguish dividing cells that are not visible on the image reconstructed with the one-wavelength algorithm (red circles in Figs. 2a and 2b). The dramatic change in cell shape at mitosis results in a strong phase shift that exceeds 2π. This phase wrapping is not present on the phase images reconstructed from the one-wavelength algorithm, as this signal vanishes
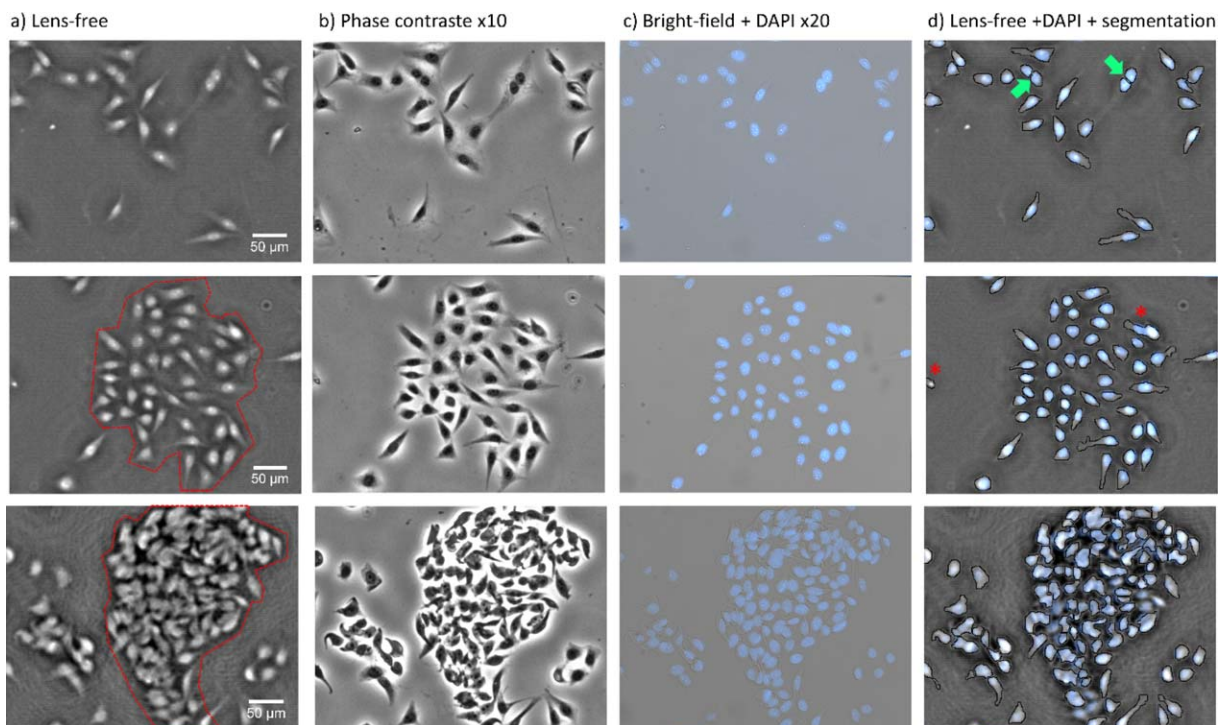
Figure 3. (a) Reconstructed phase image of a fixed cell culture of HeLa cells for three different cell densities. The local cell densities range from top to bottom, respectively, 184, 703, and ~2,500 cells/mm^2. The last two densities are measured in the cells cluster outlined with a red dashed line. (b) Acquisition of the same region as in (a) acquired with a phase contrast microscope (×10 magnification, Nikon Eclipse). (d) Acquisition of the same region as in (b) acquired with a fluorescence microscope (×20 magnification, Zeiss Axioplan). The staining of the nuclei with DAPI is shown as a blue overlay on top of the bright-field acquisition (gray). (d) The reconstructed phase images shown in (a) with the DAPI staining overlaid in blue and the automatic cell segmentation as solid black lines. The green arrows point dividing cells that are correctly segmented. The red asterisk show the mistakes of the automatic lens-free cell segmentation when compared to the nuclei stained with DAPI acquisition. There is one false positive (on the left) and one false negative (on the right). [Color figure can be viewed at wileyonlinelibrary.com]

with the positive constraint applied on the phase during the iterative reconstruction process. Thus the multiwavelength algorithm allows for accurate recognition of the cell mitosis that gives access to the study of the cell cycle (see below for further analysis of the cell cycle). In the following we will show the reconstructed phase images corrected with a phase unwrapping, for example, the negative phase values found within the segmented cells are increased by 2π.

In order to assess the spatial resolution of multiwavelength lens-free microscopy with respect to the imaging of transparent objects, we used a microscope glass slide engraved with the USAF1951 pattern at a depth of approximately 300 nm (Supporting Information Fig. S5). The smallest recognizable element is the element 5 of Group 7 (spatial frequency of 203 line pairs/mm, a width of 2.5 μm), which corresponds to a full-pitch spatial resolution of approximately 5 μm.

Cell Population and Single Cell Analysis

The reconstructed phase image of adherent cell culture from the multiwavelength holographic reconstruction presents a high contrast, and is almost free of "twin image" artifacts (Figs. 1 and 2). We designed a segmentation algorithm adapted to the reconstructed phase images taking advantage of their high-contrast (see Supporting Information

Fig. S6). The comparison of the automated lens-free segmentation to a phase contrast acquisition of fixed HeLa cells shows that the lens-free segmentation is missing some cytoplasm regions but detects well all nuclear regions (Supporting Information Fig. S6def). The main part of the phase signal is located in the nuclear region, where most of the non-aqueous material is present. Thus, automated lens-free segmentation is close to the nuclear region. This was confirmed with a comparison between the automated lens-free segmentation and a fluorescence acquisition of the nuclei stained with DAPI on HeLa cells (Supporting Information Fig. S6def). In particular for denser regions, the segmented area is very close to the nuclear region, while for several isolated cells some of the cytoplasm is included in the segmentation. Overall, we find that for HeLa cells, the segmentation works well up to local densities of approximately 700 cells/mm^2 (Fig. 3). At larger densities, the segmentation tends to blend different cells (Fig. 3). With fibroblast cells with a more complex morphology than HeLa cells, we found that at a cell density of 350 cells/mm^2 (Supporting Information Fig. S7), the lens-free automatic cell counting presents a true positive rate (specificity) of 98% (true positives = 252, false negatives = 5) and a positive predicted value (precision) of 92% (true positives = 252, false positives = 19).
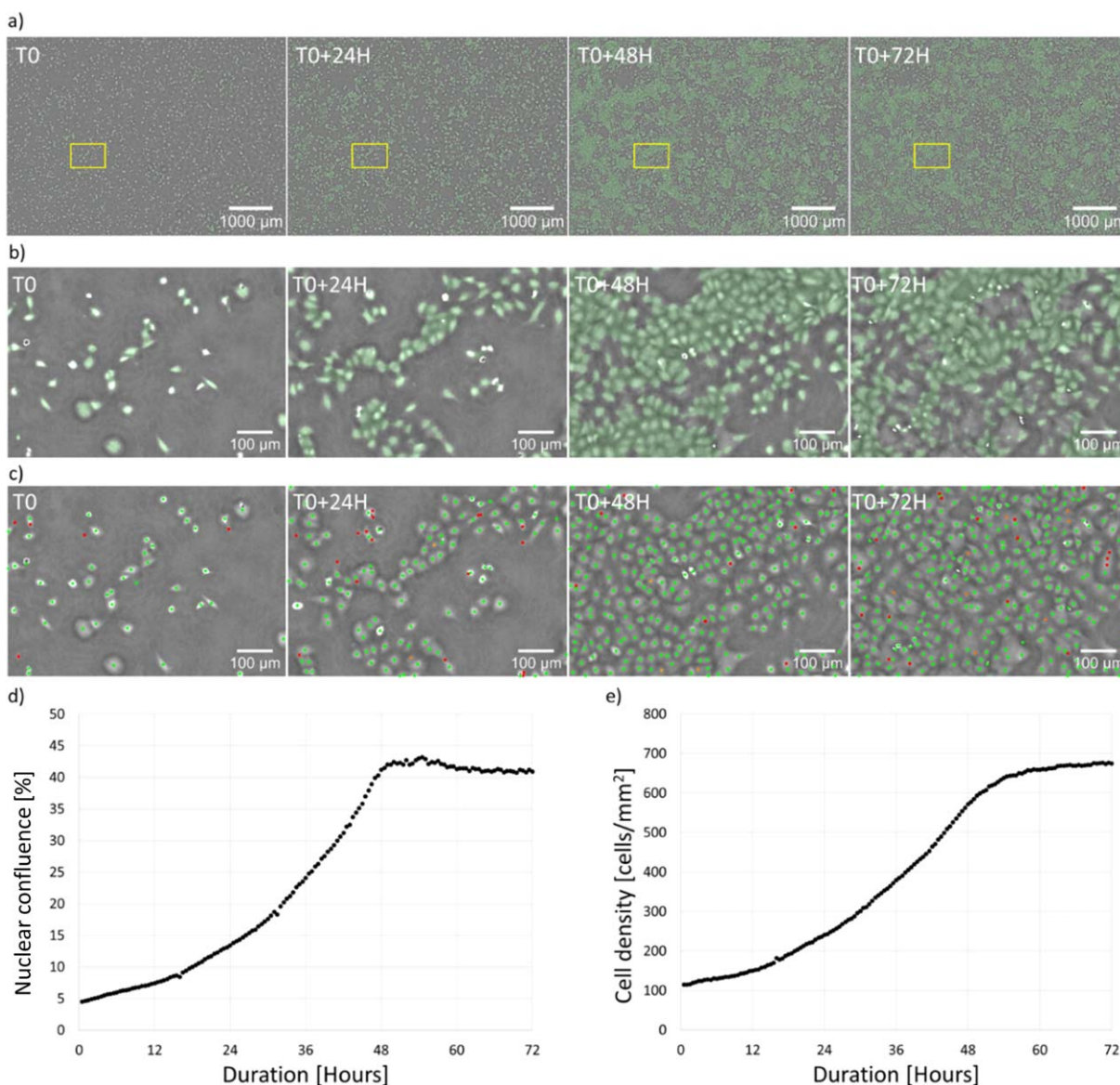
Figure 4. Cell proliferation assays performed on a culture of A549 cells. (a) Full field of view time-lapse acquisition of a culture of A549 cells over three days acquired by lens-free microscopy (blue channel). The segmented cell areas are overlaid in green. (b) Cropped images [yellow box in (a)]. (c) Cell count performed on the lens-free acquisition with a gray level watershed algorithm. Green spots correspond to proper cell detection. The manual corrections are shown with orange spots and red spots, corresponding to false negatives and false positives, respectively. The number of false negatives is low while the number of false positives is larger but does not excess 5% of the total number of cells at the highest cell density. (d) Nuclear confluence, given as the percentage of surface occupied by the nuclear regions of the cell population, as a function of time. As detailed in the text, the nuclear confluence is quantitative only at high densities. In this regime, this definition has the advantage to go beyond the classical confluence which saturates at 100% while the cell density can still increase. (e) Cell density as a function of time. [Color figure can be viewed at wileyonlinelibrary.com]

Figure 4 shows the result of the lens-free automatic cell counting applied to the time-lapse acquisition of a culture of A549 cells performed over three days. This proliferation assay shows the number of detected cells increasing from 3,400 to 19,900 over a FOV of 29.4mm^2. The latter cell count corresponds to a cell density of about 675 cells/mm^2 (Fig. 4e). Locally the measured cell density is as large as 1,650 cells/mm^2 and it does not visibly impede the quality of the reconstruction (Fig. 4c). In addition to the automatic cell counting algorithm we designed a specific watershed gray-level segmentation algorithm (see full description in Supporting Information). It is then possible to extract several metrics describing the cell morphology, namely its surface area (S), major axis length (L), minor axis length (l), cell orientation (θ), and aspect ratio (L/l). For example, the latter could be an indicator of cell polarization. The sum of the cellular areas would give the confluence. Importantly, the lens-free signal is mainly coming from the nuclear region, and the segmented areas fall close to be the nucleus (Fig. 3). This is less valid for isolated cells as the segmented areas take some cytoplasm. Nevertheless, at higher densities, we can
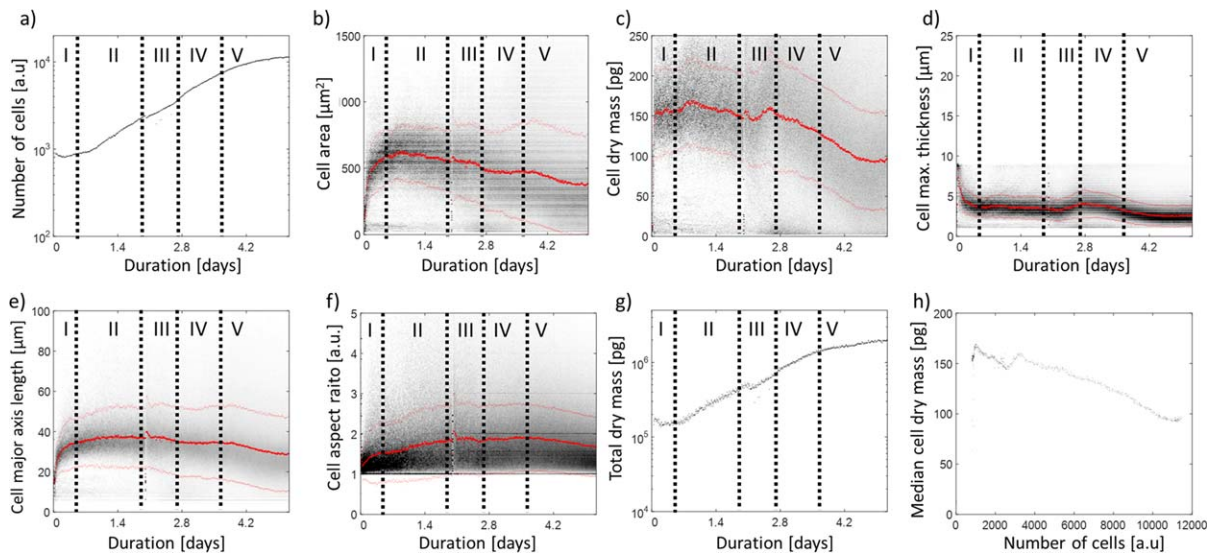
Figure 5. Data analysis of a 5 days lens-free timelapse of 3T3 fibroblast cells. (a) Total number of cells counted in the full field of view of 29.4 mm^2 as a function of time. (b–f) Scatterplot as a function of time of, respectively, the cell segmented area (b), the cell dry mass (c), the cell maximum thickness (d), the cell major axis length (e), and the cell aspect ratio (f). Every scatter plot compiles about 3.3 × 10^6 measurements. They are normalized to the number of cells present in the field of view. The median curve is plotted in red and ±1σ standard deviation curves are plotted with red dashed lines. In (f) the cell aspect ratio is given as the ratio between the minor and major axis lengths. The phases I–V separated by black dash-lines correspond to different kinetic phases of the cell cultures, and are described in the main text. (g) Total dry mass calculated as the integral of the cell dry mass over the full field of view of 29.4 mm^2 as a function of time. (h) Plot of the mean cell dry mass as a function of the total number of cells. The mean cell dry mass is calculated as the total cell dry mass (g) divided by the total number of cells (a). [Color figure can be viewed at wileyonlinelibrary.com]

define a "nuclear confluence," which corresponds to the percentage of total area occupied by the nuclear regions. It has the advantage of going beyond the classical confluence which saturates at 100% while the cell density can still increase. Cells would reach a plateau of nuclear confluence, corresponding to a homeostatic cell density. Limiting factors for the cell density might be contact inhibition of proliferation or cell extrusion, processes which could be studied on large cell populations with lens-free microscopy. The value of the homeostatic density is expected to be cell type dependent, and can be viewed as quantification of the cell type, mesenchymal, squamous epithelium, or columnar epithelium. For A549 cells, a squamous epithelial cell line, this plateau is at about 40% (Fig. 4d).

The phase recovered from lens-free microscopy is proportional to the optical density of the traversed layer. This optical density is dominated by the density of non-aqueous molecules, and the integral of the phase across the segmented cell yields a measurement of the cell dry mass (CDM) (19–21):

$$CDM = \iint \frac{\lambda \varphi(x,y)}{2\pi\alpha(x,y)} \delta x \delta y \qquad (3)$$

where $\varphi(x,y)$ is the reconstructed phase shift (21), λ the wavelength, and α the specific refractive index which relates the refractive index change to dry mass (19). Proteins and nucleic acids are the main contributions to the total cell dry mass, and have a similar specific refractive index. Hence it is reasonable to take an average value for the specific refractive index, $\alpha = 1.8 \times 10^{-4}$ m^3/kg (19,21). In the same vein, the cell

maximum thickness h can be calculated from the maximum of the phase shift in the segmented cell:

$$h \approx \frac{\lambda}{2\pi\Delta n} \max [\varphi(x,y)] \qquad (4)$$

with $\Delta n = n - n_0$ the difference in refractive index between the cell and the cell culture media, that we take in the following to be 0.025. Cell thickness is given here as a qualitative measure since we take an arbitrary value for the difference in refractive index. Nevertheless it allows us to probe the evolution in a large cell population and observe differences between and within cell lines.

In contrast, the lens-free cell dry mass measurement can be considered as quantitative. Indeed, we compared lens-free measurement to DHM measurements, a reference quantitative imaging microscope (19,22–26), and found a good agreement in between the CDM found by the two techniques (Supporting Information Fig. S8). Comparing the cell dry mass measured with lens-free microscopy and DHM over 306 fixed HeLa cells, we found a ratio approximately 0.91 between the two measurements and a coefficient of determination R^2 of approximately 0.93 (Supporting Information Fig. S8). Lens-free phase imaging does share a similar limitation with DHM (26); the holographic reconstruction process cannot properly reconstruct mitotic when light propagates with multiple reflections/diffractions within the rounded cell. As a result, the phase is overestimated at mitosis and so are the cell dry mass and cell thickness measurements. The same limitations impede the reconstruction of overlapped 3D cell organizations.

Figure 5 shows the computation of all aforementioned metrics as a function of time for a cell culture of fibroblasts performed over 4.5 days. The number of cells in the FOV increases from 1,000 to 11,000 (Fig. 5a). This results in a large dataset of 3.3×10^6 detected cells featuring their coordinates and morphological features, that is, cell area, cell volume, cell dry mass, cell maximum thickness, major axis length, and aspect ratio. It is thus possible to study the kinetics of a cell culture with unprecedented statistics. The initial phases of a cell dispersion can be clearly distinguished, that is, cell-substrate adhesion, cell spreading, cell proliferation, and confluency. We can distinguish five phases in the evolution of the different quantities; (i) phase I corresponds to the spreading of the cells on the substrate; (ii) phase II is the cell proliferation before media change; (iii) phase III is the altered cell proliferation after media change; (iv) phase IV is the normal cell proliferation; and (v) is when the density is high enough to observe the effect of contact inhibition of proliferation.

As the cells adhere to the substrate (phase I in Figs. 5a–5f), the median cell area increases from approximately 200–500 μm^2 in about 8 hours (Fig. 5b) and the median cell thickness decreases by a factor of two (Fig. 5d). Conversely, we found that the measured median cell dry mass remained constant during the first hours (Fig. 5c). While actively spreading, fibroblasts adopted an elongated shape with an average length of 40 μm along their major axis (Fig. 5e) and an aspect ratio of almost 2 (Fig. 5f). Again we insist that this corresponds roughly to the length of the nuclear region, which largely dominates the signal. The aspect ratio can be regarded as a hallmark of cell polarization, and this polarization may increase in time due to secretion of extracellular matrix on glass, a well-known trait of fibroblasts (27,28).

Once the cells have fully adhered, the population grows exponentially (Fig. 5a), as expected in normal culture conditions. This is accompanied by a decrease of area and of length (Figs. 5b–5e). The maximal thickness stays more or less constant (Fig. 5d), which is expected below extreme densities as the maximum height is then governed by the cell nucleus (29). The aspect ratio increases until a certain density, then reaches a plateau, and finally decreases at last (phase V in Fig. 5f). The onset to the decrease may be linked with the jamming transition (30).

More subtle changes can also be observed, for instance the variations that occurs at and after media replacement. In Figure 5, media change was performed after 2.1 days, and led to immediate small variations in cell major axis length, cell maximum thickness and cell eccentricity (Figs. 5d–5f). This may be connected to a small osmotic shock at media change. In the following 8 hours, the median cell dry mass and cell height are increasing (Figs. 5c and 5d), and the total dry mass increases at a similar pace (Fig. 5g). We also observe that the proliferation rate decreases slightly in this regime (Fig. 5a). To understand this, we hypothesize that the cell are partially starved before media change, some cells being locked in the G0 phase (31). At media change, the cell population is partially synchronized (31) and thus cell proliferation is altered during the following hours. Then a boost in cell proliferation occurs at 2.8 days, 15 hours after media change. This corresponds to the duration of the cell cycle of fibroblast cells. Cell proliferation lasted about 3.5 days before plateauing at 350 cells/mm^2 (Fig. 5a).

At high density, and in particular for mesenchymal cells such as fibroblasts, contact inhibition of proliferation will stop cell division. This halt is accompanied by a decrease in cell dry mass, by a factor of 1.5 (Fig. 5c), as expected for cells stuck in the quiescent phase, for which global protein synthesis is largely reduced (32). A reduced protein synthesis could also occur due to a culture media starving of the cells which is also visible before the culture media change (Fig. 5c). Overall this would lead to a tendency for the cells to be smaller in terms of CDM at high densities, which we observe in Figure 5h. We note that the decrease in CDM may be partially linked to a decreases of the segmented area to the nuclear region, but since the nucleus signal largely dominates the overall signal, we expect this effect to be small. At last, we remark that after Day 4 most of the measurements become noisy (Fig. 5e). This defines a heuristic criteria for the degradation of the quality of the reconstructions at high density. The multiwavelength holographic reconstruction still performs well at this large cell density but the cell segmentation become unprecise and noise is thus observed in, for example, the cell dry mass measurements after Day 4 of the experiment (Figs. 5g and 5h). This set an upper limit for the automatic lens-free cell segmentation algorithm which is efficient up to a cell density of approximately 350 cell/mm^2 for fibroblasts cells, in agreement with Supporting Information Figure S7.

Cell Tracking

In order to further extend the analysis of the datasets produced by lens-free video microscopy, we performed cell tracking [Trackmate ImageJ plugin (33)] on the time lapse acquisitions, and combined the tracking data with previously measured cell morphological features (Fig. 6). The cell tracking is robust, and enables us to extract 15,000 tracks that last more than 12 hours and 4,000 tracks that last more than 32 hours for a 5 days experiment (Figs. 6a–6c). The tracking can be further analyzed using devised quantitative tracking measures (34,35), such as the mean square displacement, the total, the net distances traveled, and the associated persistence. It is therefore possible to observe and quantify different types of cell motion between different cell lines or even within one cell line. A549, Huvec, and primary fibroblasts have a super-diffusive random walk with a power law exponent of about 1.5, typical for motile cells (Supporting Information Fig. S9). On the contrary, the weakly-adherent THP1 macrophages have a more varied motility. From the study of the mean-square displacement, we are able to distinguish different motility patterns inside a cell cultures, including a large sub-population of sub-diffusive cells, a smaller set of near-diffusive cells, and only a few super-diffusive cells (Supporting Information Fig. S9).

In addition to the cell migration study, we combined the cell tracks information and the metrics for every single cell that we mentioned previously. Figures 6d–6h shows as an
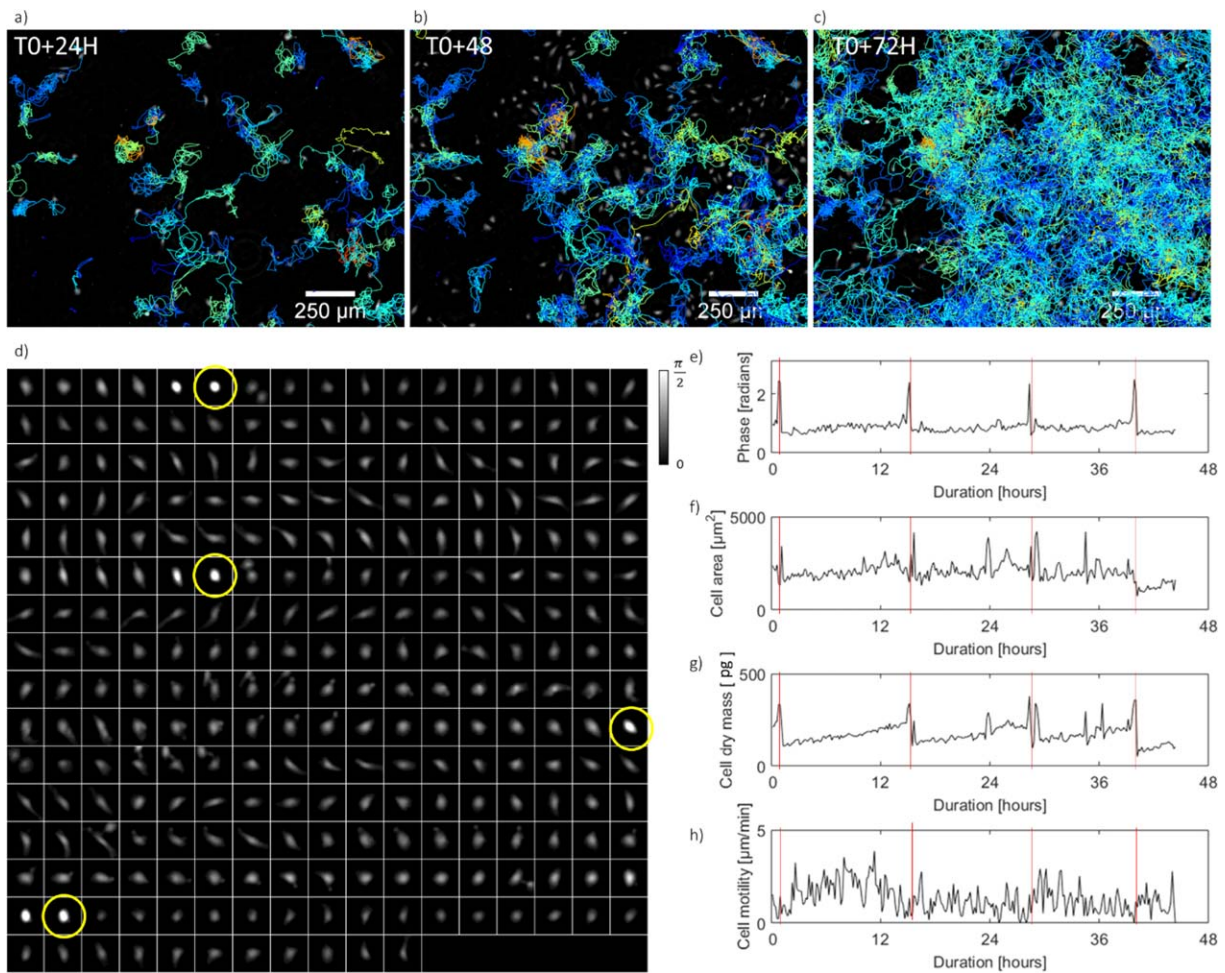
Figure 6. Cell tracking analysis of a four days acquisition of primary human umbilical vein endothelial cells (10 min frame interval), using the ImageJ plugin Trackmate. (a), (b), and (c) show the measured tracks at T0 + 24 h, T0 + 48 h, and T0 + 72H, respectively (crop of the full field of view of 29.4 mm^2). Only tracks lasting >12 hours are plotted. The color of the tracks corresponds to their total duration. In the full field of view, there are 2,200, 7,800 and 18,000 tracks at T0 + 24 h, T0 + 48 h, and T0 + 72H, respectively. (d) Time lapse acquisition of a primary human umbilical vein endothelial cell tracked over 44 h at 10 min interval. Each cropped image shows a reconstructed phase image of the segmented cell (81 μm × 81 μm). Phase unwrapping is performed by adding 2π to the negative phase values within segmented cells. (e) Plot of the cell phase signal at the centroid as a function of the experiment time. The phase signal presents a sharp peak increase corresponding to a cell division [red circles in (d) and red lines in (e–h)]. (g) Plot of the cell area as a function of the experiment time. Cell area is calculated after cell segmentation of the cell phase image (a). (g) Time evolution of the cell dry mass calculated from the integral of the phase over the segmented cell area according to Eq. (3). (h). Plot of the cell motility as a function of time. [Color figure can be viewed at wileyonlinelibrary.com]

example the analysis of a single primary human umbilical vein endothelial cell track lasting 44 hours that exhibits four cell divisions. The first mitosis occurs at T0 + 4 h (yellow circle box in Fig. 6a, frames 25–26). Three other cell divisions are at T0 + 18.5 h, T0 + 31.7 h, and T0 + 43.3 h, respectively. During mitosis, a cell goes through a major structural reorganization leading to cell rounding (36), which coincides with a sharp peak increase of the phase signal measured at the cell centroid (Fig. 6e). The signal to noise ratio of this peak is large (17 ± 7) and cell divisions can be detected with a high significance, with a 5σ threshold applied on the phase signal (red lines in Fig. 6b). In order to assess the efficiency of this cell division detection method, we have automatically generated a series of time-lapse sequences with 6 frames centered on the

detection of the cell division at interval of 10 minutes, and checked manually whether the daughter cells are visible (Supporting Information Fig. S10). Performing this task over 234 time-lapse sequences we found only 4 phase peaks that were not corresponding to a cell division. The automatic detection of cell division thus provides a robust measure of the cell division time, and consequently an accurate measurement of the period in between two divisions, that is, the cell cycle duration. From the cell tracking analysis of a 4 day culture of HUVEC cells, we extracted 1,280 cell cycles. We found that the distribution of the cell cycle duration is near Gaussian (Supporting Information Fig. S11a) with a mean of 13 h and a relative standard deviation of 15% (standard deviation divided by the mean of the distribution). Between two cell

divisions it is also possible to quantify the distributions of the initial cell dry mass measured just after division, the cell final cell dry mass and the average cell growth rate during the cycle. We found an average ratio of approximately 1.86 between the final and initial cell dry mass (Supporting Information Fig. S11b) and an average growth rate of approximately 5.5 pg/h (Supporting Information Fig. S11c).

Conclusion

We have demonstrated that a multiwavelength reconstruction algorithm using three well separated wavelengths allows for an efficient and faithful reconstruction of the phase image of densely packed cells. We could image with high contrast cell colonies at densities up to approximately 700 cells/mm^2 over a field of view of 29.4 mm^2, with local densities as high as 1,650 cells/mm^2. The phase image quality is sufficient to provide robust automatic cell segmentation and tracking up to densities of 350 cells/mm^2. Very large datasets can be gathered to study the motility and morphology of individual cells in a cell culture. We show as well that multiwavelength lens-free microscopy is a quantitative phase imaging technique, which gives access to the time evolution of the cell dry mass. In particular, it allows accurate determination of the mitosis, and the monitoring of the intra-cycle cell growth. Overall, multiwavelength video lens-free microscopy provides a simple yet performant platform to monitor large cell colonies over several days, and perform downstream label-free automated cell segmentation and cell tracking.

Acknowledgments

Literature Cited

1. Marrison J, Räty L, Marriott P, O'Toole P. Ptychography–a label free, high-contrast imaging technique for live cells using quantitative phase information. Sci Rep 2013; 3:2369.

2. Tian L, Liu Z, Yeh LH, Chen M, Zhong J, Waller L. Computational illumination for high-speed in vitro Fourier ptychographic microscopy. Optica 2015;2:904.

3. Im JIK, Enley BEMH, Im CHHK, Enry HA, Ester L, Ang CHY. Incubator embedded cell culture imaging system (EmSight) based on Fourier ptychographic microscopy. Biomed Opt Express 2016;7:1–8.

4. Repetto L, Piano E, Pontiggia C. Lensless digital holographic microscope with light-emitting diode illumination. Opt Lett 2004;29:1132–1134.

5. Greenbaum A, Luo W, Su TW, Göröcs Z, Xue L, Isikman SO, Coskun AF, Mudanyali O, Ozcan A. Imaging without lenses: Achievements and remaining challenges of wide-field on-chip microscopy. Nat Methods 2012;9:889–895.

6. Mudanyali O, Oztoprak C, Tseng D, Erlinger A, Ozcan A. Detection of waterborne parasites using field-portable and cost-effective lensfree microscopy. Lab Chip 2010; 10:2419–2423.

7. Fienup JR. Phase retrieval algorithms: A comparison. Appl Opt 1982;21:2758–2769.

8. FournierFournel CT, Ducottet C. Twin-image noise reduction by phase retrieval in in-line digital holography. Opt Photon 2005;5914:59140J.

9. Pliakis D, Minardi S. Phase front retrieval by means of an iterative shadowgraphic method. J Opt Soc Am A Opt Image Sci Vis 2009;26:99–107.

10. Kesavan SV, Momey F, Cioni O, David-Watine B, Dubrulle N, Shorte S, Sulpice E, Freida D, Chalmond B, Dinten JM, et al. High-throughput monitoring of major cell functions by means of lensfree video microscopy. Sci Rep 2014;4:5942.

11. Kesavan SV, Navarro FP, Menneteau M, Mittler F, David-Watine B, Dubrulle N, Shorte SL, Chalmond B, Dinten J, Allier CP. Real-time label-free detection of dividing cells by means of lensfree video-microscopy. J Biomed Opt 2014;19:36004.

12. Momey F, Coutard JG, Bordy T, Navarro F, Menneteau M, Dinten JM, Allier C. Dynamics of cell and tissue growth acquired by means of extended field of view lens-free microscopy. Biomed Opt Express 2016;7:512–524.

13. Pushkarsky I, Lyb Y, Weaver W, Su T, Mudanyali O, Ozcan A, Di Carlo D. Automated single-cell motility analysis on a chip using lensfree microscopy. Sci Rep 2014;4:4717.

14. Bishara W, Su TW, Coskun AF, Ozcan A. Lensfree on-chip microscopy over a wide field-of-view using pixel super-resolution. Opt Express 2010;18:11181–11191.

15. Greenbaum A, Zhang Y, Feizi A, Chung P, Luo W, Kandukuri SR, Ozcan A. Wide-field computational imaging of pathology slides using lens-free on-chip microscopy. Sci Transl Med 2014;6:267ra175.

16. Su TW, Seo S, Erlinger A, Ozcan A. High-throughput lensfree imaging and characterization of a heterogeneous cell solution on a chip. Biotechnol Bioeng 2009;102: 856–868.

17. Sanz M, Picazo-bueno JA, García J, Micó V. Improved quantitative phase imaging in lensless microscopy by single-shot multi-wavelength illumination using a fast convergence algorithm. Opt Express 2015;23:2367–2375.

18. Latychevskaia T, Fink HW. Solution to the twin image problem in holography. Phys Rev Lett 2007;98:1–4.

19. Zangle T, Teitell M. Live-cell mass profiling: An emerging approach in quantitative biophysics. Nat Methods 2014;11:1221–1228.

20. Reed J, Chun J, Zangle TA, Kalim S, Hong JS, Pefley SE, Zheng X, Gimzewski JK, Teitell MA. Rapid, massively parallel single-cell drug response measurements via live cell interferometry. Biophys J 2011;101:1025–1031.

21. Popescu G, Park Y. Optical imaging of cell mass and growth dynamics. Am J Physiol Physiol 2008;02114:538–544.

22. Magistretti P, Colomb T, Marquet P, Rappaz B, Magistretti PJ, Cuche E, Emery Y, Colomb T, Depeursinge C. Digital holographic microscopy: A noninvasive contrast imaging technique allowing quantitative visualization of living cells with subwavelength axial accuracy. Opt Lett 2005;30:468–470.

23. Popescu MS, Ikeda G, Dasari T, Feld RR. Diffraction phase microscopy for quantifying cell. Opt Lett 2006;31:775–777.

24. Wang Z, Millet L, Mir M, Ding H, Unarunotai S, Rogers J, Gillette MU, Popescu G. Spatial light interference microscopy (SLIM). Opt Express 2011;19:2643–2648.

25. Sridharan S, Mir M, Popescu G. Simultaneous optical measurements of cell motility and growth. Biomed Opt Express 2011;2:2815–2820.

26. Sung Y, Tzur A, Oh S, Choi W, Li V, Dasari RR, Yaqoob Z, Kirschner MW. Size homeostasis in adherent cells studied by synthetic phase microscopy. Proc Natl Acad Sci 2013;110:16687–16692.

27. Frantz C, Stewart KM, Weaver VM. The extracellular matrix at a glance. J Cell Sci 2010;123:4195–4200.

28. De Wever O, Demetter P, Mareel M, Bracke M. Stromal myofibroblasts are drivers of invasive cancer growth. Int J Cancer 2008;123:2229–2238.

29. Neelam S, Hayes PR, Zhang Q, Dickinson RB, Lele TP. Vertical uniformity of cells and nuclei in epithelial monolayers. Sci Rep 2016;6:19689.

30. Bi D, Lopez JH, Schwarz JM, Manning ML. A density-independent rigidity transition in biological tissues, Nat Phys 2015;11:1074–1079.

31. Pardee AB. A restriction point for control of normal animal cell proliferation. Proc Natl Acad Sci U S A 1974;71:1286–1290.

32. Pereira SFF, Gonzalez RL, Dworkin J. Protein synthesis during cellular quiescence is inhibited by phosphorylation of a translational elongation factor. Proc Natl Acad Sci U S A 2015;112:E3274–E3281.

33. Chenouard N, Smal I, de Chaumont F, Maška M, Sbalzarini IF, Gong Y, Cardinale J, Carthel C, Coraluppi S, Winter, M, et al. objective comparison of particle tracking methods. Nat Methods 2014;11:281–289.

34. Mokhtari Z, Mech F, Zitzmann C, Hasenberg M, Gunzer M, Figge MT. Automated characterization and parameter-free classification of cell tracks based on local migration behavior. PLoS One 2013;8:e80808.

35. Meijering E, Dzyubachyk O, Smal I. Methods for cell and particle tracking. Methods Enzymol 2012;504:183–200.

36. Zlotek-Zlotkiewicz E, Monnier S, Cappello G, Le Berre M, Piel M. Optical volume and mass measurements show that mammalian cells swell during mitosis. J Cell Biol 2015;211:765–774.